

UCLA

UCLA Previously Published Works

Title

Optical System Design for Noncontact, Normal Incidence, THz Imaging of in vivo Human Cornea

Permalink

<https://escholarship.org/uc/item/84z7r5dh>

Journal

IEEE Transactions on Terahertz Science and Technology, 8(1)

ISSN

2156-342X

Authors

Sung, Shijun
Dabironezare, Shahab
Llombart, Nuria
[et al.](#)

Publication Date

2018

DOI

10.1109/tthz.2017.2771754

Peer reviewed



HHS Public Access

Author manuscript

IEEE Trans Terahertz Sci Technol. Author manuscript; available in PMC 2019 January 01.

Published in final edited form as:

IEEE Trans Terahertz Sci Technol. 2018 January ; 8(1): 1–12. doi:10.1109/TTHZ.2017.2771754.

Optical System Design for Noncontact, Normal Incidence, THz Imaging of *in vivo* Human Cornea

Shijun Sung,

UCLA Dept. of Electrical Engineering, Los Angeles, CA 90095

Shahab Dabironezare,

Center for Wireless Systems and Technology, TU Delft, Netherlands

Nuria Llombart,

Center for Wireless Systems and Technology, TU Delft, Netherlands

Skyler Selvin,

UCLA Dept. of Electrical Engineering, Los Angeles, CA 90095

Neha Bajwa,

UCLA Dept. of Bioengineering, Los Angeles, CA 90095 USA

Somporn Chantra,

UCLA Dept. of Ophthalmology, Los Angeles, CA 90095 USA

Bryan Nowroozi,

UCLA Dept. of Bioengineering, Los Angeles, CA 90095

Mimeo Labs Inc, Santa Monica, CA 90404 USA

James Garritano,

UCLA Dept. of Bioengineering, Los Angeles, CA 90095 USA

Jacob Goell,

UCLA Dept. of Bioengineering, Los Angeles, CA 90095 USA

Alex Li,

UCLA Dept. of Bioengineering, Los Angeles, CA 90095 USA

Sophie X. Deng,

UCLA Dept. of Ophthalmology, Los Angeles, CA 90095 USA

Elliott Brown,

Wright State University Dept. of Electrical Engineering, Dayton, OH 45435 USA

Warren S. Grundfest, and

UCLA Dept. of Electrical Engineering, Los Angeles, CA 90095

UCLA Dept. of Bioengineering, Los Angeles, CA 90095 USA

Personal use is permitted, but republication/redistribution requires IEEE permission. See <http://www.ieee.org/publicationsstandards/publications/rights/index.html> for more information.

phone: 858-663-1823; fax: 310-206-2105; zdeis@seas.ucla.edu.

Zachary D. Taylor

UCLA Dept. of Electrical Engineering, Los Angeles, CA 90095

UCLA Dept. of Bioengineering, Los Angeles, CA 90095 USA

Abstract

Reflection mode Terahertz (THz) imaging of corneal tissue water content (CTWC) is a proposed method for early, accurate detection and study of corneal diseases. Despite promising results from *ex vivo* and *in vivo* cornea studies, interpretation of the reflectivity data is confounded by the contact between corneal tissue and dielectric windows used to flatten the imaging field. Herein, we present an optical design for non-contact THz imaging of cornea. A beam scanning methodology performs angular, normal incidence sweeps of a focused beam over the corneal surface while keeping the source, detector, and patient stationary. A quasioptical analysis method is developed to analyze the theoretical resolution and imaging field intensity profile. These results are compared to the electric field distribution computed with a physical optics analysis code. Imaging experiments validate the optical theories behind the design and suggest that quasioptical methods are sufficient for designing of THz corneal imaging systems. Successful imaging operations support the feasibility of non-contact *in vivo* imaging. We believe that this optical system design will enable the first, clinically relevant, *in vivo* exploration of CTWC using THz technology.

Index Terms

Biological and medical imaging; THz imaging of cornea; medical diagnostics; clinical instruments

I. INTRODUCTION

Corneal disorders, such as Fuchs' endothelial dystrophy [1], keratoconus [2], pseudophakic bullous keratopathy and graft rejection [3, 4], are characterized by increased corneal tissue water content (CTWC) and subsequent swelling of the cornea, leading to chronic vision impairment and often requiring surgical intervention. Corneal disorders affect large populations worldwide especially that of elderly [5]. It is believed that abnormal CTWC is a key clinical manifestation of endothelial malfunctions and corneal dystrophies [6–10]. Because abnormal CTWC is an important diagnostic target for assessing the extent of tissue damage *in vivo* [6–10], quantifying and tracking CTWC can (1) provide a better understanding of the formation, development, and progression of these disorders; and (2) become a clinically useful method for early diagnosis and assist in the choice and timing of interventions. However, accurate and non-invasive *in vivo* measurement of CTWC remains elusive.

Terahertz (THz) imaging is a promising method for the sensing and imaging of CTWC due to the homogeneity of bulk corneal tissue and relative lack in physiologic variations in corneal topography compared to other structures in the body. However, despite the acquisition of clinically relevant data from *ex vivo* and *in vivo* cornea, interpretation of the results has been confounded by contact between cornea and field flattening dielectric windows that are required in standard flat-field THz imaging methods [11, 12].

In this work, we describe reflective terahertz (THz) imaging optical principles that use a combination of planar and off-axis parabolic (OAP) mirrors to scan a beam at the normal incidence across the surface of cornea while keeping the source, detector, and patient stationary. This method acquires an image of a spherical surface with an arbitrary radius of curvature by an orthographic projection of the spherical surface to Cartesian coordinates. The design enables non-contact imaging of corneal reflectivity and avoids deformations of the cornea, which was a critical confounder in our previous work [11, 12].

The following sections introduce the design and simulation of scanning optics for non-contact CTWC imaging of human cornea. Imaging principles, quasioptical modeling, and physical optics modeling are presented. The quasioptical modeling treats the OAP mirror as an ensemble of thin lenses of varying effective focal lengths. The accuracy of this quasioptical technique is assessed with a physical optics simulation code. A prototype imaging system is presented and was used to evaluate the utility of the presented optical simulations.

II. Motivation for current work

In previous studies [11–13], we investigated the utility of THz and millimeter wave imaging and sensing to track changes in CTWC. A rabbit model study (n=5) was designed to mimic disease-relevant CTWC perturbations. A dehydration protocol was applied to one cornea of each animal and the subsequent, expected rehydration was observed over a 90-minute period. During this time window, central corneal thickness (CCT) measurements were acquired with an ultrasound pachymeter (current clinical standard), and the corresponding THz reflectivities were acquired with a 100 GHz (narrowband) reflectometer and ~525 GHz (broadband) imaging system. The protocol included the application of a 12 μ m thick Mylar window to gently flatten the cornea and provide a planar surface for both systems.

The experiment revealed a strong positive correlation between increasing CCT and increasing 100 GHz reflectivity; both consistent with the intended increase in CTWC. However, the 525 GHz imaging data did not demonstrate a statistically significant increase or decrease in reflectivity and produced a limited correlation with the millimeter wave and the CCT measurement [11, 12]. An electromagnetic modeling of this problem indicated that *in vivo* cornea is a lossy etalon at millimeter wave and THz frequencies and, thus, its spectral properties are a complex coupling of CTWC and CCT [11, 12]. Model based analysis suggested that the protocol most likely modified the thickness of the cornea while leaving the aggregate CTWC relatively unperturbed, thus resulting in a resolvable “etalon effect” at 100 GHz and an apparent absence of etalon at 525 GHz. It is likely that the contact pressure of the window altered the CCT while the stream of air produced negligible variation in CTWC.

These experiments confirmed weaknesses in the exploration of THz imaging for CWTC diagnostics with current techniques. First, active imaging of the corneal surface is difficult with simple x–y scanning techniques. The corneal surface is only ~10 mm in diameter *en face* and nearly spherical with a mean radius of curvature of ~ 8 mm [14]. This geometry constrains measurements to the central apex of the cornea when using conventional, planar

raster-scanning [11]. Second, all current clinically accepted techniques of determining CTWC *in vivo* are based on thickness measurements that extrapolate CTWC from CCT [15]. Application of a dielectric field flattening window confounds CCT-to-CTWC mapping and perturb measured THz reflectivity. Considering these shortfalls, it is apparent that THz imaging of CTWC requires an improved THz imaging method that can acquire reflectivity maps of the cornea *in vivo* without contact.

To address these needs, we have designed, constructed, and characterized a system that acquires reflectivity maps of the cornea without contact. The system architecture was motivated by two key observations: (1) The cornea is nearly a perfect hypo hemisphere with respect to a THz wavelength and the person-to-person variations of corneal curvature are relatively small; (2) The *en face* diameter of the cornea is also relatively consistent across the adult population. The target curvature and field of view can be assumed a priori with a high degree of confidence. Therefore, corneal imaging is unique amongst all THz medical imaging applications and allows the system design to accommodate only a very limited set of use cases.

III. Spherical properties of the cornea

The anterior cornea (surface) is aspherical where the deviation from an ideal sphere increases toward the periphery [16]. Human cornea is also astigmatic, demonstrating different curvature and, hence, optical power as a function of cross-sectional meridian angles [17]. Characterization of corneal topology is important for interventions such as Laser-Assisted in situ Keratomileusis (LASIK) and Photorefractive Keratectomy (PRK). Topological maps can be obtained with Videokeratography [18] or Scheimpflug photography [19] techniques which interpret the surface height measurements in refractive power at each local surface. In particular, Videokeratography [20] can be used to construct dioptric power maps from corneal surface height data, which can be further fitted to a parametric surface to analyze higher-order surface features from disease or refractive surgery [21]. However, despite the maturity of topology mapping technology, there is no standardized method for analyzing topographic information [22]. Therefore, the following analysis is performed to characterize physiologic variations of anterior corneal surface.

Corneal surface data is decomposed to into a set of concentric rings centered at the corneal apex. Fourier decomposition analysis was utilized to explore the deviations between average human cornea topology and an ideal sphere [22, 23]. The fundamental mode (first term in the Fourier series expansion) is attributed to de-centration (Figure 1(a)), and the second term is attributed to “regular” astigmatism (Figure 1(b)). The RoC deviation data in Figure 2 represents the expected geometric variation from an ideal sphere. Higher order Fourier terms are grouped together as “higher order surface irregularities” and are shown to contribute much less to the overall corneal shape than either decentration or astigmatism individually. In general, the Fourier coefficients increase for equal height contour lines further from the corneal apex.

In [22], corneal surface curvature measurements are reported as diopters (D) across the meridian cross-section as a function of radial distance from the center of the cornea and the

meridian angle. The diopter values are averaged and converted to an expected RoC deviation using equation (1) where P_{typical} is the focusing power of a cornea representative of typical population ($P_{\text{typical}} = 44\text{D}$), P_{measured} is the data from [22], n is the refractive index of the cornea ($n = 1.376$), and r is the resulting standard deviation in the RoC.

$$\Delta r = (n - 1) \left(\frac{1}{P_{\text{measured}}} - \frac{1}{P_{\text{typical}}} \right) \quad (1)$$

The average RoC deviation from the first term in the series (decentration), the second term in the series (astigmatism) and the higher order terms are displayed in Figure 2 for healthy eyes (N=25), Keratoconic eyes (N=13), and grafted cornea (N=20) [22]. The format represents the expected geometric variation from an ideal sphere. Data for endothelial dystrophies, such as Fuchs, was not available during the preparation of this manuscript. However the expected deviation arising from dystrophies is expected to much less than Keratoconus thus the pathologies in Figure 2 serve as sufficient upper bound.

For normal, healthy eyes, decentration produces a mean RoC displacement deviation of ~ 0.05 mm, regular astigmatism is slightly higher at ~ 0.08 mm, and the sum total of higher modes contributes a negligible ~ 0.015 mm. Keratoconus, a condition where the cornea thickens and the CCT increases at a rate faster than the periphery [2, 24, 25], exhibits mean RoC displacement deviations up to ~ 0.4 mm. Finally, for grafted cornea, where a patient's diseased cornea has been removed and replaced with a donor cornea [4], the mean RoC displacement deviation arising for decentration, astigmatism, and higher order irregularities, are ~ 0.3 mm, ~ 0.35 mm, and ~ 0.08 mm, respectively.

It is instructive to view this RoC curvature variation with respect to a free space wavelength of 0.462 mm (650 GHz), the center wavelength of the system in section X (Figure 10). When normalized to illumination wavelength, the corneal radius of curvature is ~ 8 mm / 0.462 mm = 17.32λ . Assume that the variations described by the decentration, astigmatism, and higher order irregularities are uncorrelated and that total standard deviation can be computed as the square root of the sum of squares of each individual standard deviation. Then, the resulting RoC variations are following: Normal, healthy cornea = $17.32\lambda \pm 0.21\lambda$, Keratoconus $17.32\lambda \pm 1.16\lambda$, and grafted cornea = $17.32\lambda \pm 1.01\lambda$, corresponding to coefficients of variance ($100 \cdot \sigma/\mu$) of 1.21%, 6.69% and 5.83% respectively. Hence, with respect to the 650 GHz illumination, the corneal surface can be considered an ideal sphere with maximum expected deviations approximately one free space wavelength.

IV. Spherical Surface Imaging

A. Spherical Surface Scanning Principle

Imaging of a spherical surface is performed by positioning the CoC of the target (cornea) coincident with the focal point of an OAP mirror, and then transmitting a collimated illumination beam into the mirror clear aperture (CA), parallel to the CA normal (Figure 3).

The focused radiation is normal to the spherical surface and, in the limit of geometric optics, has a phase front curvature equal to the spherical surface RoC. The reflected, diverging beam is re-collimated by the OAP mirror and arrives coincident with the transmitted beam path. Modulating the transverse location of the collimated beam while maintaining a path parallel to the plane of mirror's clear aperture sweeps the location of the illumination spot on the spherical surface, and an image can be constructed (Figure 3). The retro-directive nature of this arrangement is compatible with any transceiver design that can multiplex/demultiplex the input and output beams using, e.g., a wire grid, thin film, or polarizing beam splitter.

This beam scanning technique accomplishes spherical surface (θ, ϕ) scanning by the geometrical projection of the target's spherical surface into the planar coordinate system (x, y) in the mirror clear aperture. This is a restatement of the Fourier-Transform property of an optical focusing element as demonstrated with a 90° off-axis parabolic mirror (OAP) in Figure 3 where transverse locations R_k and d_k are mapped to angular locations θ_k and ϕ_k respectively. Unlike the Mercator projection which transforms the surface from spherical coordinates via a cylindrical projection to rectilinear coordinates [26], this method performs conformal mapping from spherical coordinates via projection by a paraboloid surface into a rectilinear coordinate system. Although this exact mapping operation is uncommon, it shares resemblance to the conic orthographic mapping projections in cartography, such as the Lambert Conformal Conic Projection [27].

B. Effective Imaging Optic f/# and offset

The mirror scanning solid angle can be characterized by the mirror $f/\# = f_e/A = 2f_0/A$ where f_e is the effective focal length (EFL), f_0 is the parent focal length (PFL, $f_e = 2f_0$ for a 90° OAP) and A is the CA diameter (Figure 4(a)). A human cornea spans $\sim 60^\circ$ ($\pm 30^\circ$) about its apex, thus an imaging optic should approach $f_e/A = 2\tan(30^\circ) \sim 1.15$ to span $\pm 30^\circ$ in both azimuthal (Figure 3(c)) and elevation (Figure 3(a)) about the corneal apex.

Table I lists the azimuthal and elevation angles subtended by a 90° off-axis parabolic reflector, according to commonly available $f/\#$ s from vendors. Because the focusing geometry (Figure 4) is asymmetric, the azimuthal coverage angle $(\theta_- + \theta_+)$ (Figure 4(a)) is not bisected by the 90° ray (i.e. $\theta_- > \theta_+$, $\forall f_e, A$). The 90° geometry results in the relation $\theta_+ < \delta < \phi < \theta_-$ therefore θ_+ forms the lower bound on the OAP $f/\#$. The results in Table 1 and Figure 4 that a 25.4 mm PFL, 76.2 mm CA OAP ($2 \cdot 25.4/76.2 = f/0.66$) mirror can scan the entire angular extent of the cornea.

$f/\#$ is scale invariant and does not consider the size of the target relative to the size of the focusing objective. Practical considerations restrict combinations of focal length and clear aperture to pairs that avoids positioning the apex of the cornea inside the mirror. In other words, the "flange distance" should be greater than the corneal radius of curvature: $f_e - A/2 > R_c$. The flange distance and $f/\#$ are displayed in Figure 4(c), where all combinations to the right of the $f_e - A/2 = R_c$ line yield sufficiently large offsets and all combinations to the left of the $f_e = 1.15A$ yield $f/\#$ s sufficient angular coverage. Markers representing standard, commercially available pairs of effective focal lengths and apertures are superimposed on this space with the 76.2 mm diameter mirrors indicated by the dotted contour. This work utilized a 76.2 mm diameter $f/0.66$ OAP.

V. Quasioptical Analysis

A method to implement the beam scanning described in Figure 3 utilizes a set of plane mirrors, labeled x-scan and y-scan, that translate a collimated input beam in two orthogonal directions parallel to the clear aperture plane of the OAP mirror. This concept is displayed in Figure 5 where the input and output beams are multiplexed/demultiplexed by a beam splitter that optically collocates the source and detector.

The optics are laid out in three groups which transmit and receive collimated beams: (1) Transceiver subsystem, (2) Scanning subsystem, and (3) Imaging mirror. The corneal CoC is coincident with the OAP mirror's focal point and all rays of the focused beam are orthogonal to the spherical surface. Thus, all reflected rays, independent of scan mirror position will arrive at the detector feedhorn with identical convergence angle, transverse location, and extent as demonstrated with the three-superimposed beam paths in Figure 5 (ASAP, Breault Inc.).

A. Quasioptical Analysis Setup and modeling

The imaging mirror in Figure 5 is much larger than the transverse extent of the collimated input beam ($A \gg \omega_0$). At any scan location, the beam only sees a local surface of the imaging OAP mirror, from here on referred to as sub-reflector. Therefore, the transformation of the THz beam, as a function of scan location can be approximated as the transformation by an optic whose properties represent the sub-reflector; mirror surface subtended by the beam waist. Given a reasonable input collimated beam size, the segments span moderate changes in curvature and focal distance and substantially reduced asymmetry about the beam centroid. These points suggest that the sub-reflector can be accurately modeled as a thin lens whose focal length is equal to the central beam path length from the mirror surface to the focus. This setup enables the use of quasioptical analysis with Gaussian optics and ABCD matrices to compute the resulting beam transformations as a function of scan location and, thus, the image transfer function of the imaging OAP mirror [28].

The Gaussian beam setup is displayed in Figure 6(a), where the shaded areas represents the cross sections of a cornea (8 mm RoC) and a 76.2 mm clear aperture, 25.4 mm PFL, 90° OAP mirror. Three parallel ray bundles are normal to the clear aperture plane and the corresponding sub-reflectors are represented by the darker shaded areas. A Gaussian beam can be traced through each sub-reflector using (1) the distance of free space travel between a reference plane and the mirror surface height defined by the intersection of the parabolic profile and collimated beam centroid, and (2) the effective focal length of the sub reflector defined by the line segment connecting the intersection in (1) and the effective focal point of the parent OAP mirror. This concept yields a collimated path length, focused path length, and effective focal length that are all dependent on the lateral distance (R_s) between the mirror focal point and collimated beam centroid (horizontal axis in Figure 6(a)). The problem is recast to that described by Figure 6(c). To complete the problem description, a reference plane is defined at a distance d_0 from the upper tip of the OAP represented by the dotted line in Figure 6(a). This reference plane is where the collimated beam (plane coincident with the beam waist) was launched. The collimated beam travels a distance $d(R_s) + d_0$, is focused by a thin lens of $f_c(R_s)$ and then travels $f_c(R_s) - R_c$ to a convex reflector of

radius R_C (cornea). The mirror and corneal geometry ensure normal incidence for all R_S within the clear aperture of the mirror, resulting in the beam retracing its path back through the mirror collinear with the incidence path.

$$f_e(R_S) = (4f_0)^{-1} R_S^2 + f_0 = f_e \quad (2)$$

$$d(R_S) = (4f_0)^{-1} \left[\left(2f_p + \frac{A}{2} \right)^2 - R_S^2 \right] = d \quad (3)$$

Expressions for the radially dependent focal length and beam clear aperture path length are defined in equations (2) and (3). Note that these expressions are defined for the domain $R_S \in 2f_0 \pm A/2$ and are explicitly for a 90° OAP.

$$M_{P \rightarrow C}(R_m) = \begin{bmatrix} 1 & f_e - R_C \\ 0 & 1 \end{bmatrix} \begin{bmatrix} 1 & 0 \\ f_e^{-1} & 1 \end{bmatrix} \begin{bmatrix} 1 & d+d_0 \\ 0 & 1 \end{bmatrix} \quad (4)$$

$$M_{C \rightarrow P}(R_m) = \begin{bmatrix} 1 & d+d_0 \\ 0 & 1 \end{bmatrix} \begin{bmatrix} 1 & 0 \\ f_e^{-1} & 1 \end{bmatrix} \begin{bmatrix} 1 & f_e - R_C \\ 0 & 1 \end{bmatrix} \quad (5)$$

$$M_C = \begin{bmatrix} 1 & 0 \\ 2/R_C & 1 \end{bmatrix} \quad (6)$$

$$\mathbf{M}_1 = M_{P \rightarrow C} \quad (7)$$

$$\mathbf{M}_2 = M_C M_{P \rightarrow C} = M_C \mathbf{M}_1 \quad (8)$$

$$\mathbf{M}_3 = M_{C \rightarrow P} M_C M_{P \rightarrow C} = M_{C \rightarrow P} \mathbf{M}_2 \quad (9)$$

$\mathbf{M}_1 = M_{P \rightarrow C}$ (equations (4), (7)) is the transfer matrix describing the propagation of the beam from the reference plane (P) to the cornea (C). $\mathbf{M}_2 = M_C M_{P \rightarrow C}$ (Equations (6), (8)) describes the transformation of the beam by \mathbf{M}_1 and the subsequent reflection from the

spherical reflector. The overall retrodirective transmission through the optical system is described by $\mathbf{M}_3 = M_{C \rightarrow P} M_C M_{P \rightarrow C}$ (equations (6), (9)), where the beam starts and stops at the reference plane.

$$\frac{1}{q_k} = \frac{1}{R_k} - j \frac{\lambda_0}{\pi n \omega_k} \rightarrow \frac{1}{q_0} = -j \frac{\lambda_0}{\pi n \omega_0} \quad (10)$$

$$\mathbf{M}_k = \begin{bmatrix} A_k & B_k \\ C_k & D_k \end{bmatrix} \quad (11)$$

$$q_k = \frac{A_k q_0 + B_k}{C_k q_0 + D_k} \quad (12)$$

The standard complex beam parameter relations listed in equations (10) – (12) were used to compute the spot size on target (\mathbf{M}_1), the beam radius of curvature immediately prior to (\mathbf{M}_1) and following (\mathbf{M}_2) reflection from the cornea, and the coupling coefficient between the input and output beams at the reference plane (\mathbf{M}_3). These metrics were calculated for all relevant R_s with input complex beam parameter q_0 parameterized by ω_0 and a constant $R_0 \rightarrow \infty$.

B. Spot radius on the corneal surface

The spot size on the cornea was explored as a function of input beam waist size at the reference plane and the input, collimated beam location described by its radial distance (R_s) from the focal point of the OAP mirror using equations (7) and (10) – (13). These equations characterize the spot size on a plane tangent to the corneal surface and normal to the beam centroid as depicted in Figure 6(b). Due to the relatively small extent of the focused beam with respect to the corneal RoC, the spot size computed on a plane was considered a close representation of projecting the beam on to the corneal surface and assessing the extent of the intersection contour.

$$\omega_1 = \frac{\lambda}{\pi} \left[\Re \left\{ \frac{j}{q_1} \right\} \right]^{-1} \quad (13)$$

The input Gaussian beam radius (ω_0) at the reference plane was varied from 4 mm to 12 mm and the resulting output spot radius as a function of input radius and mirror scan radius (R_s) are superimposed on the shaded outline profile of a 76.2 mm CA, 25.4 mm PFL, 90° OAP mirror length for reference. Note the dotted line style at the extreme ends of each curve. The exterior points on both ends of the curves represent the edge of the mirror CA. The interior points, located closer to the mirror axis, represent one input beam radius (ω_0) from the edge

of the mirror. In practice, diffractive effects may lead to a divergence between quasioptical analysis and realized performance for beam centroid locations outside the solid line intervals.

The 4 mm input spot size demonstrates a decreasing focused spot size ω_1 for decreasing scan radius from $R_s = 85.05$ mm down to $R_s = 35.02$ mm corresponding to a beam radii of 3.36 mm 1.96 mm respectively. The focused beam radii then increase monotonically to 2.09 mm at the near edge of the mirror ($R_s = 15.78$ mm). For small radii input beams, the combination of the sub-reflector focal length and center wavelength, results in a beam waist that occurs “outside” of the cornea for large R_s , thus the beam is diverging prior to incidence on the corneal surface. As the beam f# is decreased (decreasing R_s) and the focused path length decreases (decreasing R_s), the beam waist decreases and its location converges to the surface of the cornea. Further decreases in R_s move the beam waist to “inside” the cornea and is concomitant with an increasing convergence angle. While the focused waist continues to decrease in size, the corneal surface intercepts the beam at a distance that is increasing from the location of the waist.

This behavior is somewhat reversed for the 12 mm input radius. The spot size on the corneal surface reaches its maximum at the shortest scan radius (shortest effective focal length), $R_s = 24.25$ mm, $\omega_1 = 3.1$ mm., and its minimum at the largest scan radius, $R_s = 76.58$ mm, $\omega_1 = 1.5$ mm. Unlike the 4 mm input beam, the 12 mm input beam produces a waist that is “inside” the cornea for all R_s , and the offset between the sub-reflector focal point and waist location is small with respect to radius of the cornea (R_c) for nearly all R_s . Since the input beam is large, the effective beam f# is small and leads to large convergence angles and thus large spot sizes on the corneal surface which is located a large number of Rayleigh lengths from the focal point (i.e. $8 \text{ mm} \gg z_R$).

The intermediate input spot sizes demonstrate varying dependencies on the aforementioned factors, and it is clear by inspection of Figure 7(a) that an intermediary balances the following three competing factors:

1. Decreasing R_s decreases the effective focal length of the sub-reflector and, thus, decreases the size of the focused beam waist.
2. Decreasing R_s increases the convergence angle of the beam and can increase the beam spot size on the corneal surface depending on beam input parameters.
3. Decreasing the input beam waist decreases the convergence angle while increasing the offset between sub-reflector focal point (corneal center of curvature) and focused beam waist. This can result in an increase or decrease in the spot size on the corneal surface depending on the f/# of the OAP, the input diameter of the beam, and the wavelength.

The results in Figure 7 demonstrate a tradeoff relationship between input (ω_0) and focused (ω_1) beam radii and scan radius (R_s) which arises from characterizing the focused beam at a distance $R_c > 0$ from the geometric focal point; a factor unique to corneal imaging.

C. Beam Coupling efficiency

The 2D beam coupling coefficient beam is defined in equation (15) where the relationship between q_0 and q_3 is defined in equation (14) and constructed with M_3 from equation (9). The coupling coefficient was calculated at the reference plane and is written explicitly in terms of the input and output spot sizes and radii of curvature, which together define their respective complex beam parameters. Note that equation (15) assumes infinite reflector transverse extent and does not account for diffraction.

$$q_3 = \frac{A_3 q_0 + B_3}{C_3 q_0 + D_3} \quad (14)$$

$$K_3(q_0, q_3) = \frac{4}{\left(\frac{\omega_0 + \omega_3}{\omega_3 + \omega_0}\right)^2 + \left(\frac{\pi \omega_0 \omega_3}{\lambda}\right)^2 \left(\frac{1}{R_3} - \frac{1}{R_0}\right)^2} \quad (15)$$

The coupling coefficient as a function of mirror position and input beam diameter are displayed in Figure 7(b), which demonstrate the expected relation between input and output beam matching. As the beam input radius increases and the sub-reflector effective focal length decreases (decreasing R_s) the RoC matching between the focused beam and cornea improves, resulting in a reduced perturbation of the illumination beam and increased matching at the reference plane. The 12 mm beam ranges from 0.57 – 0.95 and the 4 mm beam ranges from 0.30 – 0.03. These results confirm a monotonically decreasing coupling efficiency for increasing input radius, independent of the input beam radius.

The source and detector mirrors in Figure 5 were oriented, with respect to the beam splitter, to maintain an “ortho” configuration [29, 30]. Similarly, the beam bath through the focused mirror was retro directive thus its beam transformation can be described as the output of two identical OAP mirrors also oriented in the “ortho” configuration. Finally, the beam patterns of the source and detector were considered identical to reflect the 26 dB feedhorns used in Section X. Due to the optical system symmetry, the similarity of the transmit and received beams at the beam splitter (reference plane) was deemed a sufficient estimate of the coupling efficiency between the detector pattern and the transformed source pattern.

D. Beam RoC and Coupling

The RoCs for pre (R_1) and post (R_2) corneal reflection are displayed in Figure 7(e) and (f) respectively and were computed with equation (16). The pre-reflection RoC are consistent with the observed behavior in the spot size characterization shown in Figure 7(a).

$$R_{1,2} = \left[\Re \left\{ \frac{1}{q_{1,2}} \right\} \right]^{-1} \quad (16)$$

The RoCs resulting from the smaller input spot sizes are asymptotic and rapidly diverge to $-\infty$ for larger mirror R_s and then should approach, from $+\infty$, $+1/R_s$. Note that in Figure 7(e) only the negative RoCs are plotted and asymptotes/asymptotic behavior were omitted for clarity. As the input spot size is increased the beam waist decreases and its location converges to the corneal CoC. While most of the focused beam RoCs appear to be asymptotic, only the RoCs computed from the 4 mm, 5 mm and 6 mm beams flip sign. These occur at $R_s = 68.17$ mm, $R_s = 75.68$ mm, and $R_s = 82.26$ mm for the $\omega_0 = 4$ mm, $\omega_0 = 5$ mm, and $\omega_0 = 6$ mm respectively. All other considered beam radii maintain focused waist location “inside the cornea” for all R_s .

The reflected beam RoC demonstrates significantly less variation than the pre-reflection RoC as a function of mirror radius R_s and exhibit positive radii (divergence) for all input beam radii and mirror scan locations. Further, the high, empirical correlation of the trends with the computed coupling coefficients suggest that the post reflection RoC is the primary determinant of the coupling efficiency in the presented optics configuration.

E. Observations

The quasioptical design and analysis space for corneal imaging is unique because (1) the target is spherical, leading to increased divergence in reflection compared to the canonical flat target and (2) the target surface is NOT located at the focal point defined by the optics or beam calculations, leading to complex beam dynamics on target.

The results suggest that for a fixed input beam radius, and optimal alignment, the signal from the near edge (small R_s) of the mirror will always be higher than the far edge of the mirror (large R_s). These observations also suggest that the imaging field may be homogenized in terms of beam radius and coupling efficiency if the input beam radius is allowed to vary as a function of R_s . Finally, the results indicate that the minimum spot size on target does not coincide with the collocation of beam waist and corneal surface for the range of parameters examined.

Note that the analysis method used in this section can be extended to remove thin lens approximation treatment of the mirror surface segment. Any propagated beam can be decomposed to include higher-order Hermite-Gaussian or Laguerre-Gaussian modes, and an augmented ray-transfer method can be applied to beam propagation, thereby accounting for the asymmetric geometry of the mirror segment [31–33].

VI. Physical Optics Analysis

The quasioptical analysis of beam propagation was compared to computations by GRASP (Ticra Inc., Copenhagen, Denmark), a physical optics code typically used in reflector antenna design [34–36]. The cornea was modeled as dielectric half sphere with a refractive index of $n = 1.376$ and a radius of 8 mm. The quasi-optical system along with the sphere are simulated by a Gaussian beam source polarized along x . The source is located at the input beam plane with a vertical distance of 74.6 mm above the center of the sphere.

A. Spot size

The focused electric field distribution was sampled in a transverse/tangent plane, located at the intersection of the beam centroid and corneal surface, for every input collimated beam radius (ω_0) and location (R_s) evaluated in Figure 7. These planes are described by the x' , and z' axes in the Figure 8(a),(f) and are defined by the rotation of the reference frame (x - y - z) about the y -axis. The input beam was TM polarized (E-field aligned with the x - z or x' - z' planes) to match the source in section X.

An example of the focused beam for the input parameters $\omega_0 = 4$ mm, $R_s = 76.9$ mm is displayed in Figure 8(a) – (c) in dB scale with accompanying scale bars indicating FOV dimensions. The E-field distribution in the x' - z' plane confirms that the focused fields is nearly Gaussian. This distribution shape was also observed on the tangent target plane (y' - z') which demonstrates vanishingly small radial asymmetry (ellipticity ~ 1) and an apparent lack of cross polarization. The predicted short Rayleigh length at $\omega_0 = 4$ mm was observed and inspection of Figure 8 (b) confirms the focused beam waist is located prior to the surface of the cornea. The nearly Gaussian field distribution was attributed to the negligible effect of reflector geometry, as the local curvature of the OAP segment, subtended by a 4 mm radius beam, for large R_s , was nearly symmetric about the beam centroid.

A complementary example of a large input beam radius ($\omega_0 = 12$ mm) paired with a short scan radius ($R_s = 24.7$ mm) is displayed in Figure 8(f)-(h). The increased beam radius and mirror curvature result in the focused beam waist lying nearly coincident with the corneal CoC/OAP focal point which is visible in the x' - z' cut in Figure 8(g). Increased diffraction and the effects of increased mirror asymmetry about the beam centroid are also apparent and manifest as multiple local extremum in the field distributions of Figure 8(g)-(h) and significant radial asymmetry in Figure 8(h).

The average spot size on target (x' - y' tangent plane) was computed numerically by obtaining the modulus of the E-field, finding the location of the peak amplitude, computing the 1/e closed contour of the modulus, and then computing the average radius of the 1/e contour. These results are superimposed with a square marker (\square) in Figure 7(a) and demonstrate good agreement between quasioptical analysis and physical optics. The level of fit is further explored in Figure 7(b) which reports the difference between quasioptical radius ($\omega_{1,q}$) and physical optics average radius ($\omega_{1,p}$): $\omega_{1,q} - \omega_{1,p}$. The spot size differential further substantiates the general correlation between decreasing spot size radius and improved goodness of fit. Additionally, the graph elucidates the increased effects of diffraction and offset reflector configuration for larger input radii (ω_0) and smaller scan radii (R_s).

B. Coupling

The electric field of the input and return beams at the reference plane were sampled for every pair of ω_0 and R_s . The magnitude of the reflected beam for the $\omega_0 = 4$ mm, $R_s = 76.9$ mm pair demonstrates a significant increase in main lobe extent compared to the initial 4 mm. This corroborates with the results obtained with quasioptical analysis that indicate substantial beam divergence over the optical path which manifests in a broad re-collimated beam radius (Figure 8(c,h)). Additionally, the multiple extremum in the wrapped phase plot

(Figure 8 (e),(j)) suggests that the reference plane is located approximately one Rayleigh length from the mirror surface corroborating a curved phased front and thus appreciable beam divergence.

The converse is true for the $\omega_0 = 12$ mm, $R = 24.7$ mm beam which demonstrates a transverse extent at the reference plane only slight larger than the initial beam. The phase plot is also more uniform with extrema spaced farther apart. These plots indicate that the reference plane is likely well within one collimated beam Rayleigh length and strongly corroborate with the quasioptical analysis.

$$\overline{K}_3 = \frac{\left| \iint (\vec{E}_{inc} \cdot \vec{E}_{ref}) dA \right|^2}{\iint |\vec{E}_{inc}|^2 dA \iint |\vec{E}_{ref}|^2 dA} \text{ where } \left\{ \begin{array}{l} \vec{E}_{inc} = \vec{E}_0 \\ \vec{E}_{ref} = \vec{E}_3 \end{array} \right\} \quad (17)$$

The coefficient quantifies the field correlation between the incident electric field at the input beam plane, \vec{E}_{inc} , and the field reflected from the cornea through the OAP up to the same input plane, \vec{E}_{ref} . This coefficient was computed with equation (17) which references the square of the inner product of the vector fields with the product of the total energy in each field. The complex vector inner product accounts for mismatch between amplitude, phase, and polarization. The coupling coefficient computations were superimposed with a square marker (\square) in Figure 7(b) and again demonstrate good agreement between quasitoptical methods and physical optics. The differential between the quasioptical coupling coefficient ($K_{3,p}$) and the physical optics coupling coefficient ($K_{3,q}$): $K_{3,p} - K_{3,q}$ is plotted in Figure 7(d) and reveals a maximum deviation of $\sim 6.5\%$ at $\omega_0 \sim 8$ mm, $R \sim 76.9$ mm. The differentials for larger input beam radii are not monotonic across the scan range and this variation is likely the result of edge diffraction and cross polarization.

IX. Beam Radius Optimization

Inspection of Figure 7(a) and the tradeoffs listed in section V.B motivate the optimization of input spot size subject to a specific resolution criterion. Two candidate metrics were considered in the following equations where ω_0 is the input collimated beam radius and ω_1 is the focused beam radius on the cornea. $R_{s,1} = 2f_0 - A/2 + \omega_0$ is the “unclipped” scan radius corresponding to the near edge of the OAP, and $R_{s,2} = 2f_0 + A/2 - \omega_0$ is the “unclipped” scan radius corresponding to the far edge of the OAP mirror.

$$\omega_0 \text{ s.t. } \omega_1(R_{s,1}, \omega_0) - \omega_1(R_{s,2}, \omega_0) = 0 \quad (18)$$

$$\omega_0 \text{ s.t. } \frac{\partial}{\partial \omega_0} \left(\frac{1}{R_{s,2} - R_{s,1}} \int_{R_{s,1}}^{R_{s,2}} \omega_1(r, \omega_0) dr \right) = 0 \quad (19)$$

Equation (18) chooses input beam diameter ω_0 such that the resulting spot sizes on the target at the extremums of the scan range $[R_{s,1}, R_{s,2}]$ are equal. The solution to equation (18) corresponds to an approximate collocation of the smallest focused spot size with the apex of the cornea, while trying to minimize the asymmetry of the spot size about the corneal apex. Equation (19) chooses a collimated beam radius where the average focused spot size at the corneal surface is minimized. The parameter space and solutions to these equations are displayed in Figure 9 using the quasioptical along with physical optics results of Figure 7(a). The cross over point of the two curves that satisfy equation (18) is denoted with the gray circle (○) marker and occurs at a collimated input waist of 6.25 mm.

The input spot size dependent behavior of the solution of the differential in equation (19) is denoted with the solid black line in Figure 9 and its minimum, which satisfies (19), is denoted by the circular marker (○) at $\omega_0 = 7.6$ mm. The physical optics derived solution is plotted with the square (□) marker. The results demonstrated good agreement and identified an optimal input radius of $\omega_0 \sim 7.0$ mm.

For current clinical practice, the corneal center provides most utility when identifying disease processes, thus justifying the metric in equation (18) [37]. However, certain corneal pathologies, e.g. corneal graft rejection, can create “edematous fronts” that can start from anywhere in the periphery and migrate across the extent of the corneal surface [4]. Detection of these features supports minimizing the spatial bias of imaging system, thus justifying the metric in (19). Note that with the optimized $\omega_0 = 7.6$ mm the focused beam waist is never coincident with the corneal surface.

X. Experimental Validation of Optical Theory

A prototype system was assembled to explore the accuracy of the quasioptical theory and physical optics simulations. The coupling coefficient was chosen as a representative test because it is dependent on four parameters: (1) input radius of curvature, (2) output radius of curvature, (3) input beam radius, and (4) output beam radius.

The matching between theoretical and experimental coupling coefficient was explored by imaging a 7.93 mm radius brass sphere. Given the lack of contrast in the target, any spatial variation in signal was attributed to the predicted, spatially varying coupling efficiency.

A. System

A prototype system, based on the optics of Figure 5, was constructed with a solid-state frequency-modulated continuous wave THz source (Amplifier-multiplier chain, Virginia Diodes, Virginia) centered at 650 GHz. The detector was a WR1.5 waveguide mounted Schottky diode detector (ZBD) (Virginia Diodes, VA) with a 500GHz-700GHz detection bandwidth. Both the source and detector were coupled to diagonal feedhorn antennas with

26 dB of gain and aperture dimensions of 2.4 mm \times 2.4 mm. To mitigate standing waves, the output was frequency modulated over \sim 2 GHz at a rate of 100 kHz, producing an RF bandwidth that exceeded the expected full etalon period of the optical path. The source was also amplitude modulated at \sim 900 Hz, and the rectified signal from the ZBD was detected with a Lock-in amplifier (Stanford Research Systems, CA) using an integration time of 3 milliseconds (ms). These parameters are summarized in the block diagram of Figure 10.

The optical layout of the system (Figure 5) used 25.4 mm PFL, 76.2 mm CA, 90° OAP mirrors to collimate radiation from the multiplier chain and focus reflected radiation into the detector aperture. The combination of feedhorn directivity and OAP PFL yielded a collimated spot 1/e field radius of \sim 10 mm as measured with a knife edge target. The imaging mirror was a 76.2 mm CA, 25.4 mm PFL OAP. Beam scanning was performed with two 50.8 mm diameter gold coated plane mirrors.

B. Image and Coupling Coefficient Fits

A THz image of the brass sphere is displayed in the inset of Figure 11 and was acquired by translating the plane mirrors with 5 mm steps. Note that this data is a mapping of the reflectivity on the sphere to the transverse coordinates of the clear aperture and thus the data was directly compared to the simulation results in Figure 7 and Figure 8. The image was masked with a circle of radius $A/2 - \omega_0$ to exclude aberrations due to beam clipping.

The inset image in Figure 11 shows a general trend of decreasing signal starting from the near edge of the mirror aperture and continuing, monotonically, to the far edge (decreasing signal for increasing scan radius). A localized increase in signal is apparent in the bottom left corner of the image, which is likely due to beam diffraction. A contour line was superimposed on the aperture diameter. The arrows on the contour line corresponds to increasing scan radius and the pixels sampled by this profile are plotted with a circular line style (○) in Figure 11.

The quasioptical (equation (15)) and physical optics simulations for an input beam radius of 10 mm are superimposed on the data in a solid line style (–) and square marker (□) respectively (obtained directly from Figure 7). The experimental data and simulation results demonstrate good agreement across the center of the masked aperture of the mirror. The minimum deviation occurs at the mirror center ($R_s = 50.8$ mm) while the maximum deviation occurs towards the mirror near edge ($R_s = 28$ mm). This indicates that diffraction may contribute to observed contrast beyond $A/2 - \omega_0$ and supports the exploration of smaller mask radii.

XI. Conclusions

This work presents a novel imaging principle and analysis method for normal incidence, non-contact THz imaging of spherical targets with applications to corneal diagnostics. An analysis of the variation in the geometric properties of the cornea was presented. It was shown that when referenced to a THz wavelength the cornea can be considered an ideal sphere; even under perturbations from corneal diseases and the effects of surgical interventions. This analysis motivated the design of a corneal imaging system that places the

corneal CoC coincident with the focal point of a low $f/\#$ OAP mirror. Transverse sweeping of a collimated beam in the clear aperture plane produces angular scanning of a focused beam along the surface of the cornea.

Quasioptical techniques were introduced that segment parabolic mirrors into an ensemble of thin lenses where the effective focal length and free space beam paths are proportional to the distance between the parent focal point and mirror clear aperture centroid. The spot size on target, radius of curvature pre and post reflection, and coupling coefficient between transmit and received beams were simulated for a single OAP reflector.

The spot size on target and quasioptical coupling coefficient were also computed with full wave physical optics and good agreement between the physical optics results and the quasioptical results was demonstrated. The imaging mirror was over dimensioned ($A \gg \omega_0$) therefore diffractive effects were limited for most of the considered input parameter space. The concurrence of the results strongly supports the use of quasioptical techniques as a design and analysis tool.

An imaging system based on Figure 5 was constructed and used to acquire images of a brass ball target with an RoC matching that of cornea. A profiles of intensity variation along the vertical diameter of the image was compared with the quasioptical and physical optics theory and good agreement was observed between image contrast and predicted coupling coefficients.

The limited variation of the shape and size of cornea among adult population is unique amongst all structures in the body and, when referenced to the typical center wavelength of a THz imaging system, even more negligible. We believe that the presented systems and analysis techniques provide a good first step towards the *in vivo* translation of this technology to human subjects.

Acknowledgments

This work is supported by the National Eye Institute (NEI) Grant# 5R01EY021590. The authors would like to thank Mr. Lu Han at Taylor and Francis for facilitating the discussions that lead to this research.

This work was supported in part by the National Eye institute under Grant Number 5R01EY021590.

References

1. Adamis AP, Filatov V, Tripathi BJ, Tripathi RAMC. Spotlight on ExhibitorsFuchs' endothelial dystrophy of the cornea. *Survey of Ophthalmology*. 1993; 38:149–168. 1993/09/01. [PubMed: 8235998]
2. Rabinowitz YS. Keratoconus. *Survey of Ophthalmology*. 1998; 42:297–319. 1//. [PubMed: 9493273]
3. Taylor DM, Atlas BF, Romanchuk KG, Stern AL. Pseudophakic Bullous Keratopathy. *Ophthalmology*. 1983; 90:19–24. 1//. [PubMed: 6338434]
4. Panda A, Vanathi M, Kumar A, Dash Y, Priya S. Corneal Graft Rejection. *Survey of Ophthalmology*. 2007; 52:375–396. 7//. [PubMed: 17574064]
5. Whitcher JP, Srinivasan M, Upadhyay MP. Corneal blindness: a global perspective. *Bulletin of the World Health Organization*. 2001; 79:214–221. [PubMed: 11285665]

6. Waring GO III, Stulting R, Street D. Penetrating keratoplasty for pseudophakic corneal edema with exchange of intraocular lenses. *Archives of Ophthalmology*. 1987; 105:58–62. [PubMed: 3541869]
7. Ytteborg J, Dohlman CH. Corneal edema and intraocular pressure: II. clinical results. *Archives of Ophthalmology*. 1965; 74:477–484. [PubMed: 5294510]
8. Waring GO, Rodrigues MM, Laibson PR. Corneal dystrophies. II. Endothelial dystrophies. *Survey of Ophthalmology*. 1978; 23:147–168. 1978/11/01. [PubMed: 310583]
9. Rodrigues MM, Krachmer JH, Hackett J, Gaskins R, Halkias A. Fuchs' Corneal Dystrophy. *Ophthalmology*. 1986; 93:789–796. 1986/06/01. [PubMed: 3526227]
10. Krachmer JH, Purcell JJ Jr, Young CW, Bucher KD. Corneal endothelial dystrophy: A study of 64 families. *Archives of Ophthalmology*. 1978; 96:2036–2039. [PubMed: 309758]
11. Taylor ZD, Garritano J, Shijun S, Bajwa N, Bennett DB, Nowroozi B, Tewari P, Sayre JW, Hubschman JP, Deng SX, Brown ER, Grundfest WS. THz and mm-Wave Sensing of Corneal Tissue Water Content: In Vivo Sensing and Imaging Results. *Terahertz Science and Technology, IEEE Transactions on*. 2015; 5:184–196.
12. Taylor ZD, Garritano J, Sung S, Bajwa N, Bennett DB, Nowroozi B, Tewari P, Sayre J, Hubschman JP, Deng S, Brown ER, Grundfest WS. THz and mm-Wave Sensing of Corneal Tissue Water Content: Electromagnetic Modeling and Analysis. *Terahertz Science and Technology, IEEE Transactions on*. 2015; 5:170–183.
13. Bennett DB, Taylor ZD, Sassoon D, Tewari P, Johnson RD, Singh R, Culjat MO, Hubschman J-P, Grundfest WS. Terahertz sensing in corneal tissues. *J Biomed Opt*. 16:8.
14. Liu Z, Huang AJ, Pflugfelder SC. Evaluation of corneal thickness and topography in normal eyes using the Orbscan corneal topography system. *British Journal of Ophthalmology*. 1999; 83:774–778. [PubMed: 10381661]
15. Li Y, Shekhar R, Huang D. Corneal Pachymetry Mapping with High-speed Optical Coherence Tomography. *Ophthalmology*. 2006; 113:792–799.e2. 5//. [PubMed: 16650675]
16. Gullstrand, A. Appendix. In: Helmholtz, HV., editor. *Handbuch der physiologischen Optik*. Vol. 1. New York, Dover: p. 351-352.
17. Srivannaboon S, Reinstein DZ, Sutton HFS, Holland SP. Accuracy of Orbscan total optical power maps in detecting refractive change after myopic laser in situ keratomileusis. *Journal of Cataract & Refractive Surgery*. 1999; 25:1596–1599. 12//. [PubMed: 10609202]
18. Bogan SJ, Waring GO III, Ibrahim O, Drews C, Curtis L. Classification of normal corneal topography based on computer-assisted videokeratography. *Archives of Ophthalmology*. 1990; 108:945–949. [PubMed: 2369353]
19. Hockwin O, Weigelin E, Laser H, Dragomirescu V. Biometry of the Anterior Eye Segment by Scheimpflug Photography. *Ophthalmic Research*. 1983; 15:102–108. [PubMed: 6877752]
20. Applegate RA, Howland HC. Noninvasive measurement of corneal topography. *IEEE Engineering in Medicine and Biology Magazine*. 1995; 14:30–42.
21. SCHWIEGERLING J, GREIVENKAMP JE. Using Corneal Height Maps and Polynomial Decomposition to Determine Corneal Aberrations. *Optometry & Vision Science*. 1997; 74:906–916. [PubMed: 9403887]
22. Hjortdal JØ, Erdmann L, Bek T. Fourier analysis of video-keratographic data. A tool for separation of spherical, regular astigmatic and irregular astigmatic corneal power components. *Ophthalmic and Physiological Optics*. 1995; 15:171–185. [PubMed: 7659417]
23. RAASCH TW. Corneal Topography and Irregular Astigmatism. *Optometry & Vision Science*. 1995; 72:809–815. [PubMed: 8587769]
24. Krachmer JH, Feder RS, Belin MW. Keratoconus and related noninflammatory corneal thinning disorders. *Survey of Ophthalmology*. 1984; 28:293–322. 1//. [PubMed: 6230745]
25. GROMACKI SJ, BARR JT. Central and Peripheral Corneal Thickness in Keratoconus and Normal Patient Groups. *Optometry & Vision Science*. 1994; 71:437–441. [PubMed: 7970558]
26. Lee LP. THE TRANSVERSE MERCATOR PROJECTION OF THE ENTIRE SPHEROID. *Empire Survey Review*. 1962; 16:208–217. 1962/01/01.
27. Snyder JP. Map projections used by the U.S. Geological Survey. *USGS Numbered Series*. 1982; 1532:101.

28. Goldsmith, P. Gaussian Beam Quasioptical Propagation and Applications Piscataway, NJ: IEEE Press; 1998.
29. Murphy JA. Distortion of a simple Gaussian beam on reflection from off-axis ellipsoidal mirrors. *International Journal of Infrared and Millimeter Waves*. 1987; 8:1165–1187. 1987/09/01.
30. Malone RM, Becker SA, Dolan DH, Hacking RG, Hickman RJ, Kaufman MI, Stevens GD, Turley WD. Design of a thermal imaging diagnostic using 90-degree off-axis parabolic mirrors. 2006:62880Z–62880Z-9.
31. Zauderer E. Complex argument Hermite–Gaussian and Laguerre– Gaussian beams. *Journal of the Optical Society of America A*. 1986; 3:465–469. 1986/04/01.
32. Siegman AE. Hermite–gaussian functions of complex argument as optical-beam eigenfunctions. *Journal of the Optical Society of America*. 1973; 63:1093–1094. 1973/09/01.
33. Pampaloni F, Enderlein J. Gaussian, hermite-gaussian, and laguerre-gaussian beams: A primer. arXiv preprint physics/0410021. 2004
34. Llombart N, Cooper KB, Dengler RJ, Bryllert T, Siegel PH. Confocal Ellipsoidal Reflector System for a Mechanically Scanned Active Terahertz Imager. *IEEE Transactions on Antennas and Propagation*. 2010; 58:1834–1841.
35. Cooper KB, Dengler RJ, Llombart N, Bryllert T, Chattopadhyay G, Mehdi I, Siegel PH. An Approach for Sub-Second Imaging of Concealed Objects Using Terahertz (THz) Radar. *Journal of Infrared, Millimeter, and Terahertz Waves*. 2009; 30:1297–1307.
36. Cooper KB, Dengler RJ, Llombart N, Thomas B, Chattopadhyay G, Siegel PH. THz Imaging Radar for Standoff Personnel Screening. *IEEE Transactions on Terahertz Science and Technology*. 2011; 1:169–182.
37. LACKNER B, SCHMIDINGER G, PIEH S, FUNOVICS MA, SKORPIK C. Repeatability and Reproducibility of Central Corneal Thickness Measurement With Pentacam, Orbscan, and Ultrasound. *Optometry and Vision Science*. 2005; 82:892–899. [PubMed: 16276321]

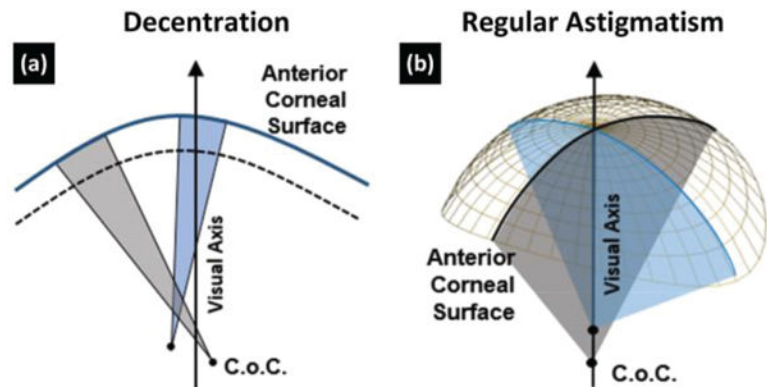


Figure 1. Corneal anatomy. The anterior and posterior surfaces are represented by the curved solid and dotted lines respectively. (a) Decentration: local surfaces may have centers of curvature (CoC), that do not lie on the central optical axis. and (b) Astigmatism: Radial asymmetry results in and focal points from different axes lying at different depths along the optical axis.

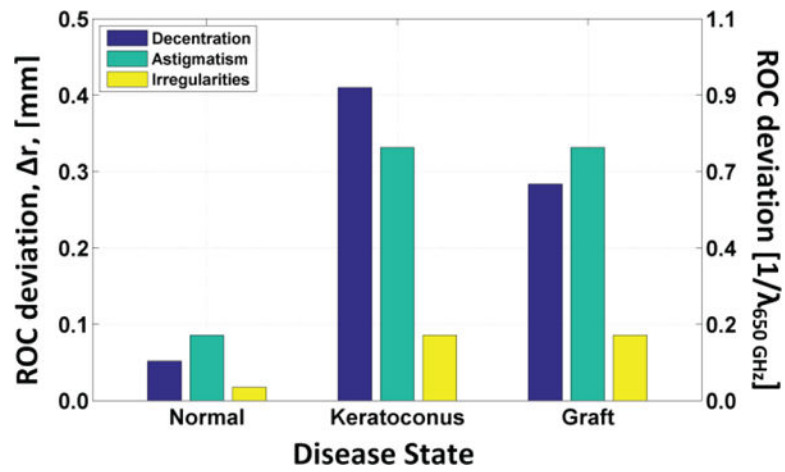


Figure 2. Average corneal RoC variation (Δr , equation (1)) for healthy cornea (left), Keratoconus (middle), and Grafted cornea (right). The contribution to overall RoC variation is decomposed into decentration, regular Astigmatism, and higher order irregularities [22]. The maximum RoC variation is less than 1λ @ 650 GHz.

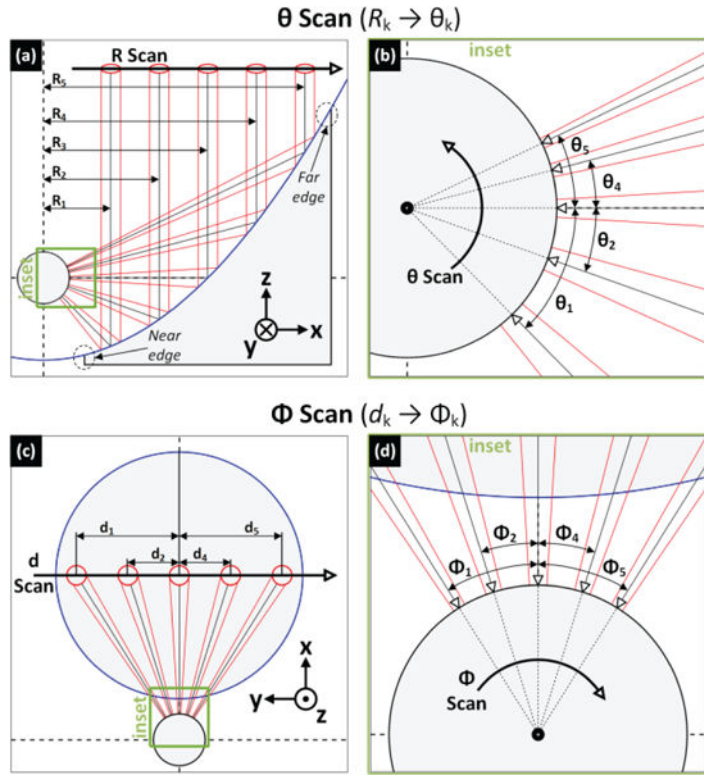


Figure 3. Mapping of transverse translation in the mirror CA plane to angular translation on the corneal surface. In (a) and (b), transverse locations R1 – R5 are mapped to angular scan locations θ_1 – θ_5 . In (c) and (d), transverse scan locations d_1 – d_5 are mapped to angular scan locations ϕ_1 – ϕ_5 . Note that the focused beam is intercepted prior to the focal point and that all beams are normal to the corneal surface.

Author Manuscript

Author Manuscript

Author Manuscript

Author Manuscript

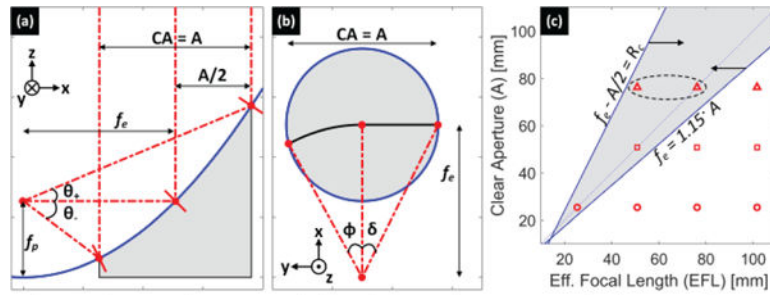


Figure 4.

Half angles of 90° OAP mirrors: ϕ , δ , θ_+ and θ_- . (a) side view. (b) Clear aperture view. (c) Design space bordered by offset $f_e - A/2 = R_c$ and $f_e = 1.15A$. Standard, commercially available mirrors indicated by [○] 25.4 mm, [□] 50.8 mm, and [△] 76.2 mm apertures.

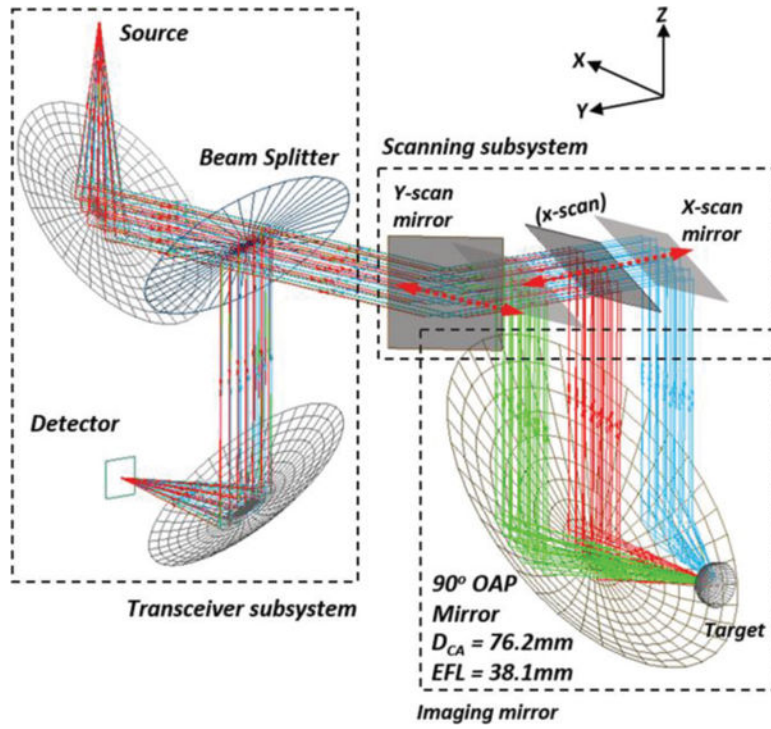


Figure 5. Imaging system design. The raypath is plotted starting from the source, then traced to the scanning mirrors (only x- scanning shown), target, and back to the detector. If the target is spherical, all rays focus to a point on the detector, invariant to scan mirror position.

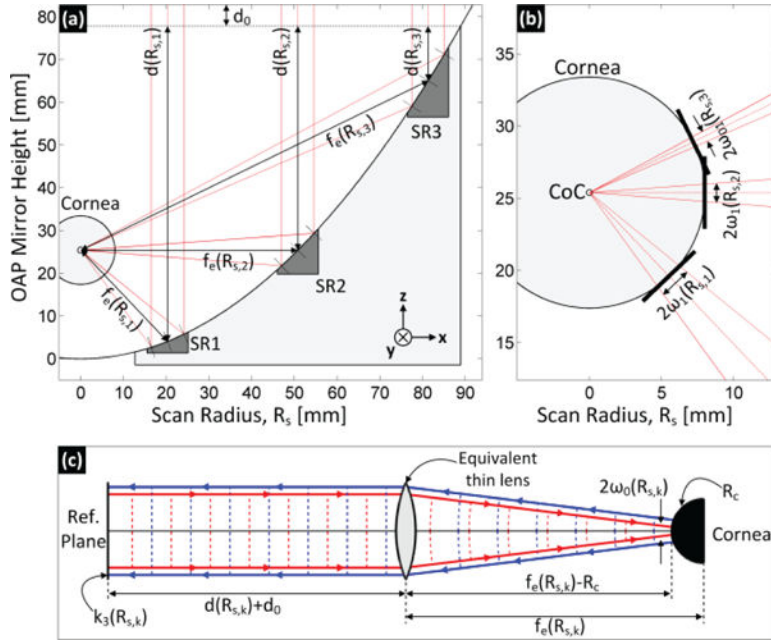


Figure 6. Raypath diagram of the beam scanning. (a) parabolic mirror segmentation location, (b) definition of reference plane tangent to the corneal surface at the intersection of beam centroid and cornea. The focused spot size was characterized on these reference planes. This is where spot size on the surface of the cornea. (c) Thin lens equivalent of the overall beam path.

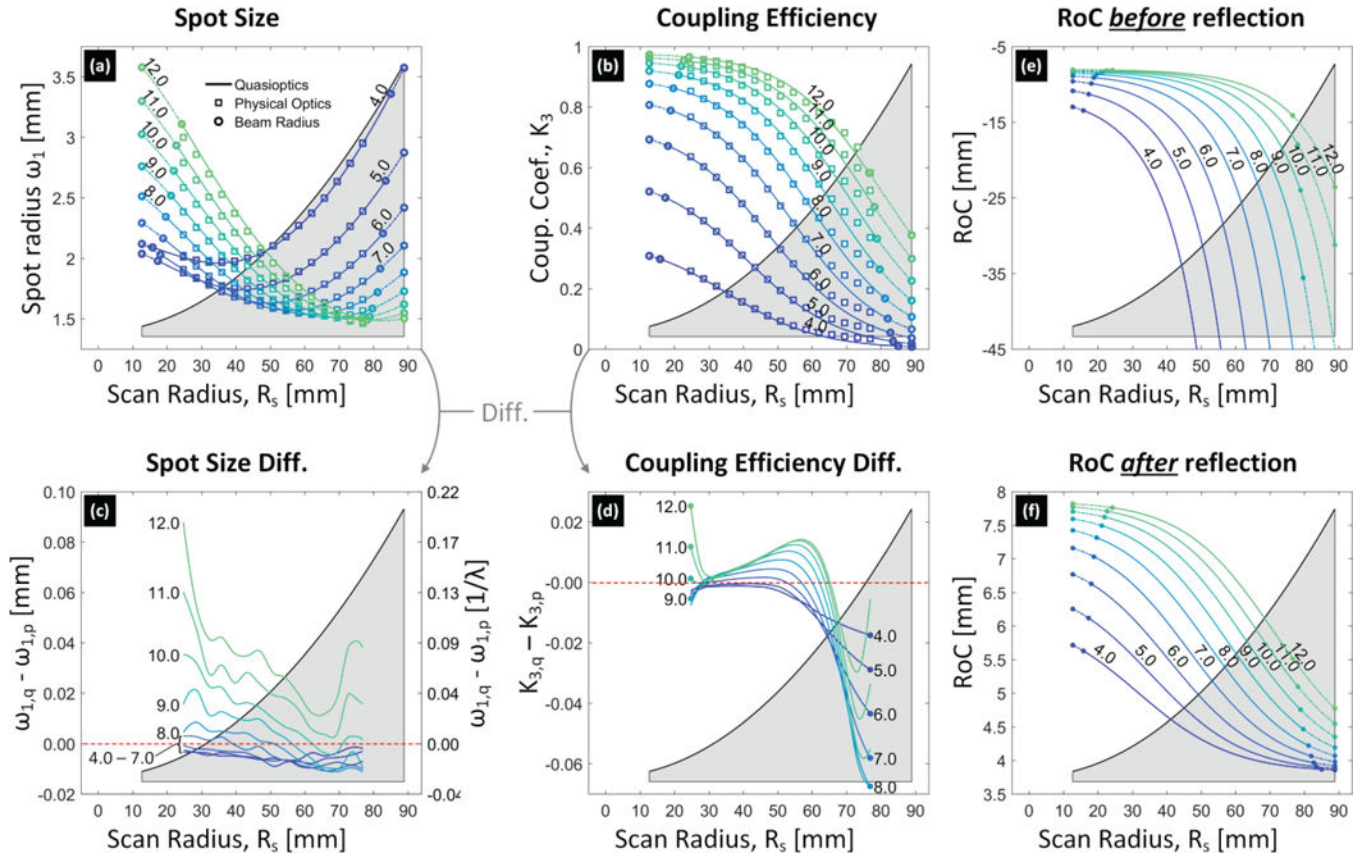


Figure 7.

Quasi-optical and physical optics computations of relevant beam parameters. The physical optics results are discussed in section VI. (a) Focused spot radius on the analysis plane (Figure 6(b)) as a function of the input beam location (R_s) over the parabolic profile of the imaging OAP mirror. Each curve represents different collimated beam radii (ω_0) ranging from 4 mm – 12 mm. A scaled overlay of parabolic cross section is shown to depict the location of the beam. (b) Coupling coefficient between the input and output beam as a function of input beam location over the parabolic profile of the imaging OAP mirror. (c) Differential between quasi-optics and physical optics computations for ω_1 . (d) Differential between quasi-optics and physical optics computations for K_3 . Radius of curvature of the beam immediately on the target surface (e) and immediately after reflection (f), as a function of the input beam radial location over the parabolic profile of the imaging OAP mirror. Strong agreement was observed between the quasi-optical analysis and physical optics computations. Maximum deviation occurs for larger input diameters near the edge of the mirror indicating diffraction.

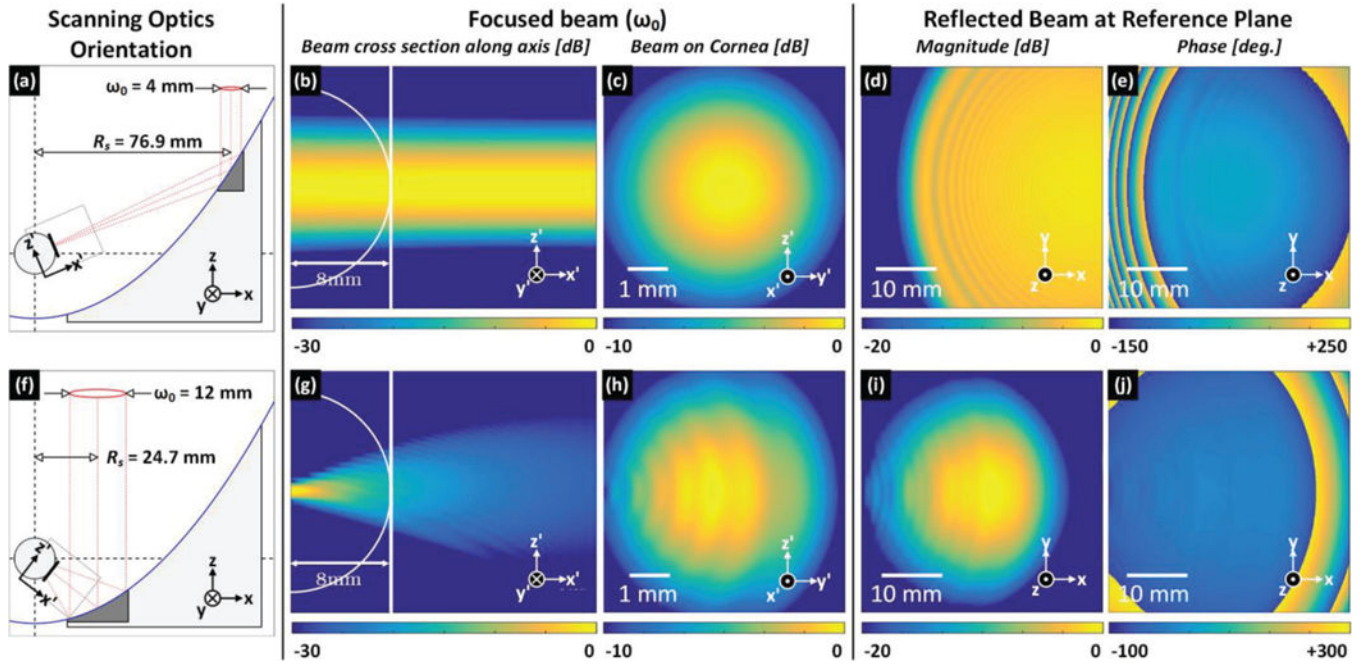


Figure 8.

(a) Layout for $\omega_0 = 4$ mm and $R = 76.9$ mm. (b) cross section of beam in the $x'-z'$ plane. section (c) beam profile on the $y'-z'$ plane tangent to the cornea and coincident with the intersection of the focused beam centroid and corneal surface. Electric field magnitude (d) and phase (e) of the beam at the reference plane ($x-y$ plane) following reflection from the cornea and recollimation from the OAP. (f) Layout for $\omega_0 = 12$ mm and $R = 24.7$ mm. (g)-(j) same as (b)-(e). Note that in configuration (a) the fields are nearly Gaussian while in configuration (f) they are not due to the offset reflector configuration and possible diffraction. Blue correspond to lower E-field amplitude and yellow corresponds to higher.

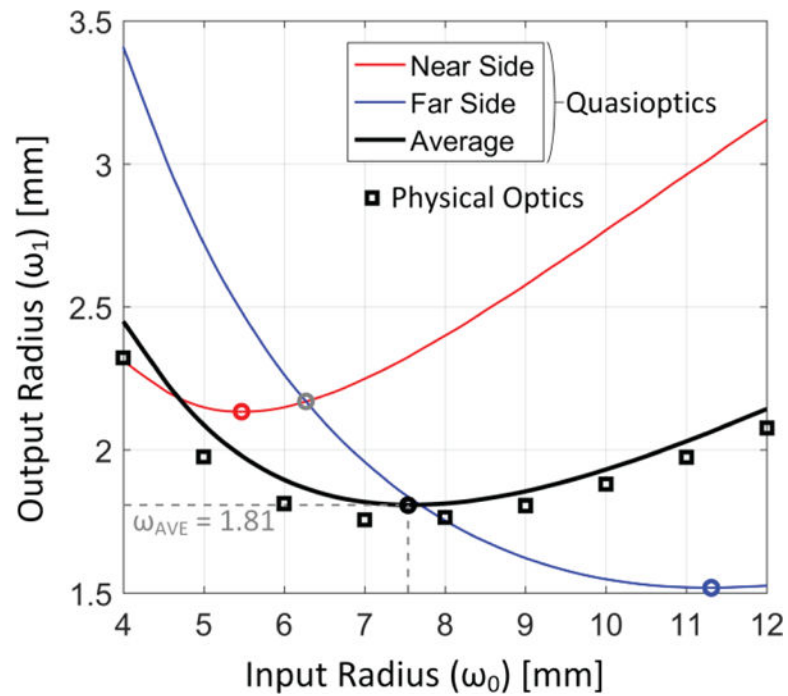


Figure 9.

Optimization space for equations (18) and (19). The intersection of the near (red) and far (blue) edge traces is the solution to equation (18). The black curve represents the argument of the derivative in equation (19) and the black circular (○) marker is the solution of equation (19). The square (□) markers were computed from the physical optics simulations.

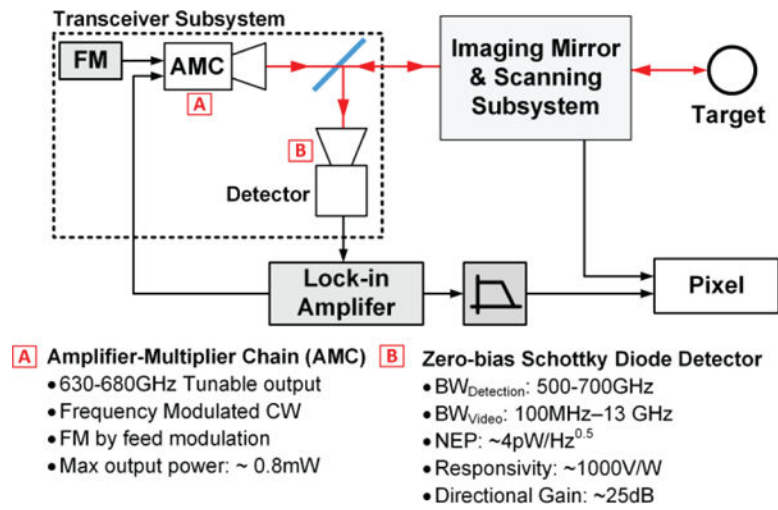


Figure 10.
Block diagram of the prototype system.

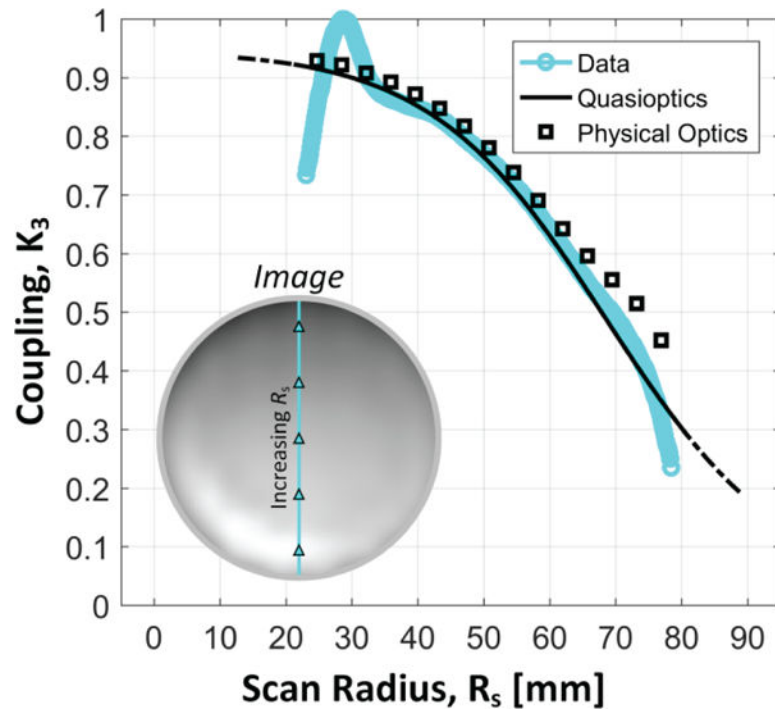


Figure 11.
Coupling calibration target with data fit to equation (15).

Table ISpherical scanning angles (deg.) by imaging reflector $f/\#$

$f/\#$ (fe/A)	0.66	1	2	3
θ_-	62.8	36.9	16.3	10.4
θ_+	30.7	22.6	12.7	8.8
ϕ	44.5	29.0	14.4	9.6
δ	37.2	26.6	14.0	9.5

Author Manuscript

Author Manuscript

Author Manuscript

Author Manuscript